

## HUBBLE SPACE TELESCOPE ADVANCED CAMERA FOR SURVEYS CORONAGRAPHIC IMAGING OF THE AU MICROSCOPII DEBRIS DISK

JOHN E. KRIST,<sup>1</sup> D. R. ARDILA,<sup>2</sup> D. A. GOLIMOWSKI,<sup>2</sup> M. CLAMPIN,<sup>3</sup> H. C. FORD,<sup>2</sup> G. D. ILLINGWORTH,<sup>4</sup> G. F. HARTIG,<sup>1</sup>  
 F. BARTKO,<sup>5</sup> N. BENÍTEZ,<sup>2</sup> J. P. BLAKESLEE,<sup>2</sup> R. J. BOUWENS,<sup>4</sup> L. D. BRADLEY,<sup>2</sup> T. J. BROADHURST,<sup>6</sup>  
 R. A. BROWN,<sup>1</sup> C. J. BURROWS,<sup>1</sup> E. S. CHENG,<sup>7</sup> N. J. G. CROSS,<sup>2</sup> R. DEMARCO,<sup>2</sup> P. D. FELDMAN,<sup>2</sup>  
 M. FRANX,<sup>8</sup> T. GOTO,<sup>2</sup> C. GRONWALL,<sup>9</sup> B. HOLDEN,<sup>4</sup> N. HOMEIER,<sup>2</sup> L. INFANTE,<sup>10</sup> R. A. KIMBLE,<sup>3</sup>  
 M. P. LESSER,<sup>11</sup> A. R. MARTEL,<sup>2</sup> S. MEI,<sup>2</sup> F. MENANTEAU,<sup>2</sup> G. R. MEURER,<sup>2</sup> G. K. MILEY,<sup>8</sup>  
 V. MOTTA,<sup>10</sup> M. POSTMAN,<sup>1</sup> P. ROSATI,<sup>12</sup> M. SIRIANNI,<sup>2</sup> W. B. SPARKS,<sup>1</sup>  
 H. D. TRAN,<sup>13</sup> Z. I. TSVETANOV,<sup>2</sup> R. L. WHITE,<sup>1</sup> AND W. ZHENG<sup>2</sup>

Received 2004 September 10; accepted 2004 October 20

### ABSTRACT

We present *Hubble Space Telescope* Advanced Camera for Surveys multicolor coronagraphic images of the recently discovered edge-on debris disk around the nearby ( $\sim 10$  pc) M dwarf AU Microscopii. The disk is seen between  $r = 0''.75$  and  $15''$  (7.5–150 AU) from the star. It has a thin midplane with a projected FWHM thickness of 2.5–3.5 AU within  $r < 50$  AU of the star that increases to 6.5–9 AU at  $r \sim 75$  AU. The disk's radial brightness profile is generally flat for  $r < 15$  AU, then decreases gradually ( $I \propto r^{-1.8}$ ) out to  $r \approx 43$  AU, beyond which it falls rapidly ( $I \propto r^{-4.7}$ ). Within 50 AU the midplane is straight and aligned with the star, and beyond that it deviates by  $\sim 3^\circ$ , resulting in a bowed appearance that was also seen in ground-based images. Three-dimensional modeling of the disk shows that the inner region ( $r < 50$  AU) is inclined to the line of sight by less than  $1^\circ$  and the outer disk by  $\sim 3^\circ$ . The inclination of the outer disk and moderate forward scattering ( $g \approx 0.4$ ) can explain the apparent bow. The intrinsic, deprojected FWHM thickness is 1.5–10 AU, increasing with radius. The models indicate that the disk is clear of dust within  $\sim 12$  AU of the star, in general agreement with the previous prediction of 17 AU based on the infrared spectral energy distribution. The disk is blue, being 60% brighter at  $B$  than  $I$  relative to the star. One possible explanation for this is that there is a surplus of very small grains compared with other imaged debris disks that have more neutral or red colors. This may be due to the low radiation pressure exerted by the late-type star. Observations at two epochs show that an extended source seen along the midplane is a background galaxy.

**Key words:** circumstellar matter — stars: individual (AU Microscopii)

### 1. INTRODUCTION

Collisions of planetesimals around a star produce dust grains, creating a debris disk that can be detected in thermal emission and scattered light. Without the continual replenishment of these grains, most of the disk will disappear because of radiation and wind pressure, Poynting-Robertson drag, grain coagulation, and tidal interactions with planets. The lifetime of such disks is not fully understood, and it may depend strongly on the luminosity of the star.

Although numerous detections and images of optically thick accretion disks have been made, only a few debris disks have been resolved. The current inventory of imaged debris disks is largely derived from *IRAS*-measured infrared excesses of stars. This list is biased toward stars of spectral types A–F because their luminosities are high enough to heat a debris disk to an *IRAS*-detectable level. More luminous stars would blow away such disks, whereas cooler stars cannot heat them enough to be detected. Most of the resolved debris disks surround A stars ( $\beta$  Pic, Vega, Fomalhaut, HD 141569A, and HR 4796), and only a few have been seen in scattered light. The sensitivity limits of *IRAS* leave uncertain the frequency of debris disks around later type stars. The disk around  $\epsilon$  Eridani, a K2 V star with one of the largest *IRAS*-measured stellar excesses, was detected by *IRAS* only because of its very close proximity (3.2 pc) to us. The *Spitzer Space Telescope* should provide a much more comprehensive catalog of disk candidates around later type stars.

There are only two M dwarfs, AU Microscopii and Hen 3-600 (Song et al. 2002), not associated with molecular clouds that have *IRAS*-measured infrared excesses. AU Mic (HD 197481, GJ 803) is a M1 Ve flare star and a BY Dra type variable ( $V_{\max} = 8.59$ ,  $\Delta V \approx 0.15$ ; Cutispoto et al. 2003). Barrado y Navascués et al. (1999) identified AU Mic as part of the  $\beta$  Pic moving group, an association of nearby (10–50 pc) young stars. It is at a *Hipparcos*-measured distance of 9.94 pc (Perryman et al. 1997) and is about 10 Myr old (Zuckerman et al. 2001). Its excess implies that AU Mic has a substantial amount of circumstellar material. These characteristics led the *Hubble Space Telescope* (HST)

<sup>1</sup> Space Telescope Science Institute, 3700 San Martin Drive, Baltimore, MD 21218.

<sup>2</sup> Department of Physics and Astronomy, Johns Hopkins University, 3400 North Charles Street, Baltimore, MD 21218.

<sup>3</sup> NASA Goddard Space Flight Center, Code 681, Greenbelt, MD 20771.

<sup>4</sup> UCO/Lick Observatory, University of California, Santa Cruz, CA 95064.

<sup>5</sup> Bartko Science and Technology, 14520 Akron Street, Brighton, CO 80602.

<sup>6</sup> Racah Institute of Physics, Hebrew University, Jerusalem 91904, Israel.

<sup>7</sup> Conceptual Analytics, LLC, 8209 Woburn Abbey Road, Glenn Dale, MD 20769.

<sup>8</sup> Leiden Observatory, Postbus 9513, NL-2300 RA Leiden, Netherlands.

<sup>9</sup> Department of Astronomy and Astrophysics, Pennsylvania State University, 525 Davey Laboratory, University Park, PA 16802.

<sup>10</sup> Departamento de Astronomía y Astrofísica, Pontificia Universidad Católica de Chile, Casilla 306, Santiago 22, Chile.

<sup>11</sup> Steward Observatory, University of Arizona, Tucson, AZ 85721.

<sup>12</sup> European Southern Observatory, Karl-Schwarzschild-Strasse 2, D-85748 Garching, Germany.

<sup>13</sup> W. M. Keck Observatory, 65-1120 Mamalahoa Highway, Kamuela, HI 96743.

Advanced Camera for Surveys (ACS) Investigation Definition Team (IDT) to include the star in its circumstellar disk imaging program.

A disk around AU Mic was recently imaged from the ground using coronagraphs (Kalas et al. 2004, hereafter KLM04; Liu 2004, hereafter L04). These images show a disk that at first glance resembles that of  $\beta$  Pic. It is viewed nearly edge-on and has a radius of at least  $21''$  (210 AU). The Keck adaptive optics image of L04 also shows small-scale variations in the midplane that might be due to localized density enhancements caused by unseen substellar companions that perturb the disk. So far, imaging within  $1''.5$  of the star has not been possible from the ground. The high resolution of ACS and its ability to see closer to the star can provide more detailed views of this disk.

## 2. OBSERVATIONS, PHOTOMETRY, AND PROCESSING

### 2.1. Observations and Calibration

The ACS IDT observations of AU Mic utilized the coronagraphic mode of the ACS High Resolution Camera (HRC), which has a pixel scale of  $\sim 25$  mas pixel $^{-1}$  and a coronagraphic field point-spread function (PSF) FWHM of 72 mas at  $I$ , 63 mas at  $V$ , and 50 mas at  $B$ . The  $r = 0''.9$  occulting spot was used for all observations. The coronagraph suppresses the diffraction pattern of the central star, reducing the surface brightness of its wings by  $\sim 7$  times. The remaining flux from the occulted source is dominated by scattered light from the telescope optics for  $r > 1''.5$  and by light diffracted by the occulting spot for  $r < 1''.5$ . The latter appears as concentric rings around the image of the spot. Because of the stability of *HST*, most of the residual light can be subtracted using an image of another star.

Since AU Mic was on the ACS IDT target list before discovery of its disk, the team's standard observation strategy for suspected disks was used: initial imaging in one filter to confirm the existence of a disk, followed later with multicolor imaging. The ACS exposures are listed in Table 1. The first images (*HST* program 9987) were taken on 2004 April 3 in filter F606W (wide  $V$ -band) and the second set (program 10330) on 2004 July 24 in F606W, F435W (ACS  $B$ ), and F814W (ACS wide  $I$ ). The telescope orientations were specified to place the disk diagonally on the detector, and the orientations of the two sets of images were separated by  $90^\circ$ . Exposures of HD 216149 ( $V = 5.4$ ) in the same filters were taken after AU Mic at both epochs for use in PSF subtraction. This star was chosen because it is bright, is of a similar color as AU Mic, and is near AU Mic on the sky so that any attitude-dependent focus variations could be minimized. In addition to the coronagraphic exposures, short, direct (noncoronagraphic) images were taken to provide photometry of the stars.

All of the images were calibrated by the *HST* pipeline. To account for vignetting around the occulting spot, the coronagraphic images were manually divided by the spot flats available from the ACS reference files page at the Space Telescope Science Institute (STScI) Web site. Because the spot varies in position over time, each spot flat was shifted to the appropriate position as listed on the ACS Web page. The duplicate exposures were combined with cosmic-ray rejection. At this stage, the images were not corrected for geometric distortion.

### 2.2. Stellar Photometry

Photometric measurements of the two stars are required to properly normalize the HD 216149 images prior to subtraction from those of AU Mic. The AU Mic fluxes were measured from the short, noncoronagraphic images using circular apertures with radii of 13 (F435W), 25 (F606W), and 30 (F814W) pixels,

TABLE 1  
AU MICROSCOPIC AND REFERENCE PSF EXPOSURES

Star	Date	Filter	Exposure (s)	Gain <sup>a</sup>	Type <sup>b</sup>
AU Mic .....	2004 Apr 3	F606W	$2 \times 0.1$	4	D
			$3 \times 750$	2	C
			$2 \times 1400$	2	C
	2004 Jul 24	F435W	$1 \times 0.1$	4	D
			$1 \times 60$	2	D
			$4 \times 1279.5$	2	C
		F606W	$1 \times 0.1$	4	D
			$1 \times 60$	2	D
			$2 \times 915$	2	C
		F814W	$1 \times 0.1$	4	D
			$1 \times 60$	2	D
			$3 \times 853$	2	C
HD 216149 .....	2004 Apr 3	F606W	$2 \times 0.1$	4	D
			$2 \times 90$	2	C
			$8 \times 225$	2	C
	2004 Jul 24	F435W	$1 \times 0.1$	4	D
			$2 \times 5$	2	D
			$2 \times 475$	2	C
		F606W	$1 \times 0.1$	4	D
			$2 \times 5$	2	D
			$2 \times 145$	2	C
		F814W	$1 \times 0.1$	4	D
			$2 \times 5$	2	D
			$2 \times 145$	2	C

<sup>a</sup> In electrons per data number.

<sup>b</sup> D = direct (noncoronagraphic), and C = coronagraphic.

increasing in size to account for the larger PSFs at longer wavelengths. The short exposures of HD 216149 were saturated. As reported by Gilliland (2004),<sup>14</sup> the well depth of an HRC pixel is  $\sim 160,000 e^-$ , which is within the 16 bit range of the electronics when a gain of  $4 e^-$  per data unit is used. Saturating the pixel does not saturate the analog-to-digital converter, so flux is not lost when a pixel saturates but instead overflows into an adjacent pixel. As Gilliland (2004) showed, in this case the counts are conserved, and summation within an aperture that has a radius that encompasses all of the saturated pixels should provide the same count rate as in an unsaturated image. The fluxes for HD 216149 in the three filters were measured using 30 pixel radius apertures, which include all of the saturated pixels.

The measured photometry for both stars were corrected to effectively infinite apertures using conversion coefficients derived from encircled energy curves of well-exposed, high-dynamic-range images of other stars. Because the AU Mic and HD 216149 measurements were made using images that had not been corrected for ACS geometrical distortion, compensation for pixel area distortion was made using the pixel area maps provided by STScI (Pavlovsky et al. 2004).<sup>15</sup> The instrumental fluxes were converted to standard  $BVI_C$  magnitudes (Table 2) using the STSDAS SYNPHOT synthetic photometry program assuming M1 V (for AU Mic) and M0 III (for HD 216149) spectra.

### 2.3. PSF Subtraction

The HD 216149 coronagraphic images were normalized to match the measured AU Mic fluxes. They were then iteratively

<sup>14</sup> ACS Instrument Science Report ISR 04-01 (Gilliland 2004), available at <http://www.stsci.edu/hst/acs/documents/isrs>.

<sup>15</sup> ACS Data Handbook (Pavlovsky et al. 2004), available at <http://www.stsci.edu/hst/acs/documents>.

TABLE 2  
AU MICROSCOPII AND REFERENCE PSF PHOTOMETRY

Star	Date	Passband	Magnitude <sup>a</sup>
AU Mic .....	2004 Apr 3	<i>V</i>	$8.63 \pm 0.03$
	2004 Jul 24	<i>B</i>	$9.96 \pm 0.05$
		<i>V</i>	$8.64 \pm 0.03$
		<i>I<sub>C</sub></i>	$6.60 \pm 0.03$
HD 216149 .....	2004 Apr 3	<i>V</i>	$5.46 \pm 0.03$
	2004 Jul 24	<i>B</i>	$6.71 \pm 0.05$
		<i>V</i>	$5.46 \pm 0.03$
		<i>I<sub>C</sub></i>	$4.05 \pm 0.03$

<sup>a</sup> Stated error includes estimate of magnitude system transformation error.

shifted by subpixel amounts via cubic convolution interpolation and subtracted from the AU Mic images until the residual scattered-light patterns were visibly minimized. This procedure appears to align the two stars to within  $\pm 0.05$  pixels, aided by the high spatial frequency streaks in the residual pattern, which

can be seen radiating from the star in Figures 1c–1f. After subtraction, the images were corrected for geometric distortion. The diffraction patterns inside and around the edge of the occulting spot were not well subtracted. Their shapes and intensities are quite sensitive to the alignment of the star behind the spot, which at worst differed by 16 mas between AU Mic and the reference PSF. They are also sensitive to focus changes and small differences between the spectra of the stars over a filter’s bandpass. Their residuals, which appear as alternating positive and negative rings, are the dominant source of error for  $r < 1''.5$ , where they create localized uncertainties of  $\pm 30\%$  on  $0''.1$  scales in the disk brightness in the F606W images. Although there are oscillations within and around the spot in both F606W images, they appear to have mean residuals near zero. However, in F814W the spot interior appears oversubtracted, and in F435W it is undersubtracted, probably because of focus mismatches. Further out, the background is dominated by scatter-subtraction residuals, which cause pixel-to-pixel errors of less than 10%.

In addition to the coronagraphic images, we also subtracted the longest noncoronagraphic exposure of HD 216149 from

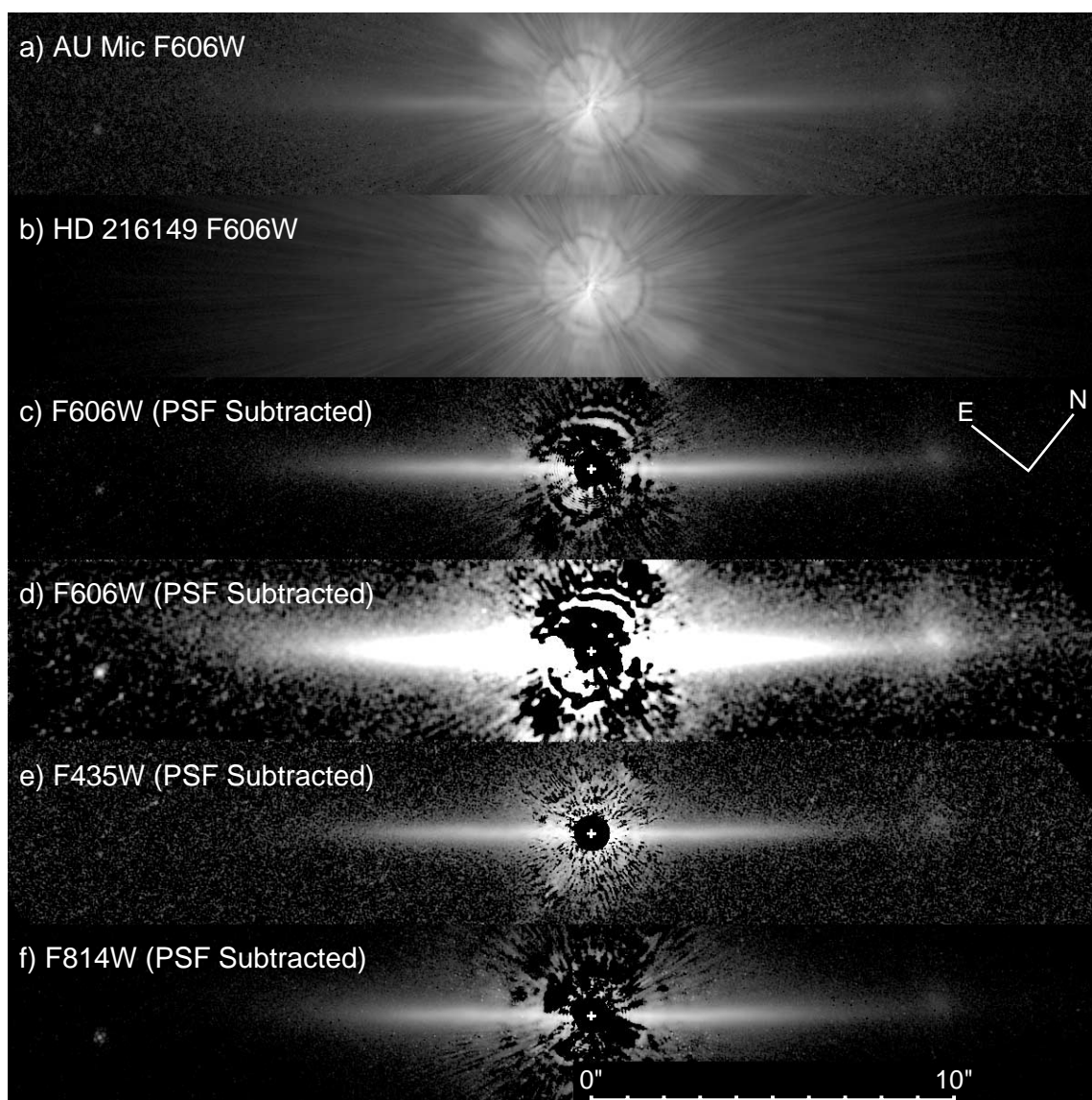


FIG. 1.—First-epoch ACS F606W coronagraphic images of AU Mic and the reference PSF star HD 216149, all displayed with logarithmic intensity scaling. Image (d) is smoothed and shown using a stronger stretch to reveal the disk at greater heights and structure associated with the galaxy superposed on the northwest extension. A background star can be seen below the southeast extension.



FIG. 2.—First-epoch ACS F606W coronagraphic PSF-subtracted image of AU Mic after subtraction of a median-smoothed copy of itself, highlighting the higher spatial frequency structures, notably the flat, sharp disk midplane (other features are noise and PSF subtraction residuals). Inverse intensity to and the same orientation as Fig. 1.

that of AU Mic. Although this clearly revealed the disk, it did not allow detection of it within  $1''$  of the star because of high subtraction residuals, providing no improvement over the coronagraphic subtractions. We also used the two F606W coronagraphic images of AU Mic to subtract each other, but because of differences in the spot positions between the two epochs, the subtraction residuals were larger than those when HD 216149 was used.

### 3. RESULTS

The AU Mic disk stands out against the background PSF structure in the ACS coronagraphic images (Fig. 1a) even before PSF subtraction. In the first-epoch F606W image (the deepest exposure), the northwestern side is detected out to the edge of the detector,  $15''.25$  ( $\sim 150$  AU) from the star, and the southeastern side to  $\sim 14''$  ( $\sim 140$  AU). The disk can be seen to a height of  $2''.5$  (25 AU) above the midplane. The observed radial and height extents in this image are sensitivity-limited. The interior of the occulting spot is filled with light that was not blocked by the spot (which is located in the aberrated *HST* beam) and was afterward modified by the corrective ACS optics. An image of the star at the spot's center allows accurate measurement of the stellar position. An extended source, which we show to be a background galaxy, can be seen superposed on the northwest midplane,  $9''.6$  from the star. A point source is also seen  $\sim 1''$  southwest of the disk midplane  $13''.7$  southeast from the star. A few background galaxies are also seen throughout the field.

The PSF-subtracted image more clearly reveals the disk (Figs. 1c–1f). Because the disk is fairly bright close to the star and the corrective optics modify the aberrated light that passes by the occulter, the disk can actually be seen inside the spot to within  $\sim 0''.75$  of the star. The residual levels indicate that using the coronagraph with PSF subtraction improves the disk-to-background contrast by  $\sim 150$  times compared with direct imaging without subtraction. Significant residuals are present in a bar of instrumentally scattered light that extends from the upper left to the lower right of the coronagraphic field, but these are

positioned away from the disk. The F606W subtractions from each epoch are of comparable quality, whereas the F814W subtraction has large residuals near and within the spot, probably because of focus differences between the two images. The residuals in the F435W image are more uniform than in the other two filters, but because AU Mic is much fainter in that pass-band, the effects of electronic noise are more significant.

The extended source detection limits in the subtracted images were estimated by adding  $1'' \times 1''$  uniform-intensity squares to the data at  $3''$  and  $9''$  from the star perpendicular to the circumstellar disk. The intensities of the squares were adjusted until they could no longer be visually detected. The derived visual detection limits are  $B = 23.3$  and  $23.5$  mag arcsec $^{-2}$  (F435W),  $V = 22.6$  and  $24.0$  (F606W), and  $I = 20.4$  and  $21.9$  (F814W) for  $r = 3''$  and  $9''$ , respectively, with estimated errors of  $\pm 0.2$  mag arcsec $^{-2}$ .

#### 3.1. Disk Morphology

Analysis of the disk morphology is largely confined to the first-epoch F606W observation, since it was the first and deepest exposure. As is shown in § 3.3, there are no significant differences in the disk morphology among the three filters.

To allow accurate measurement of the disk orientation, simple spatial filtering was applied to highlight the midplane. The image was subtracted by a copy of itself that was smoothed by a  $3$  pixel  $\times$   $3$  pixel median filter. This removed the extended vertical wings while preserving the sharp peak of the midplane seen within  $5''$  of the star (Fig. 2). A line fitted to the resulting image shows that the inner ( $r < 5''$ ) midplane is oriented at P.A. =  $128.6^\circ \pm 0.2^\circ$ . There are small ( $\sim 40$  mas) oscillations in the midplane position about this line, which passes directly through the star. Superposing this line on the original image highlights the deviation of the outer ( $r > 5''$ ) midplane from the inner (Fig. 3). At large angles, the disk looks “bowed,” an effect noted in the ground-based images and also seen in the  $\beta$  Pic disk (Kalas & Jewitt 1995). The apparent outer disk midplane measured by eye at  $r = 12''.5$  is oriented along P.A. =  $311.1^\circ \pm 0.7^\circ$  on the northwest side and P.A. =  $125.6^\circ \pm 0.7^\circ$  on

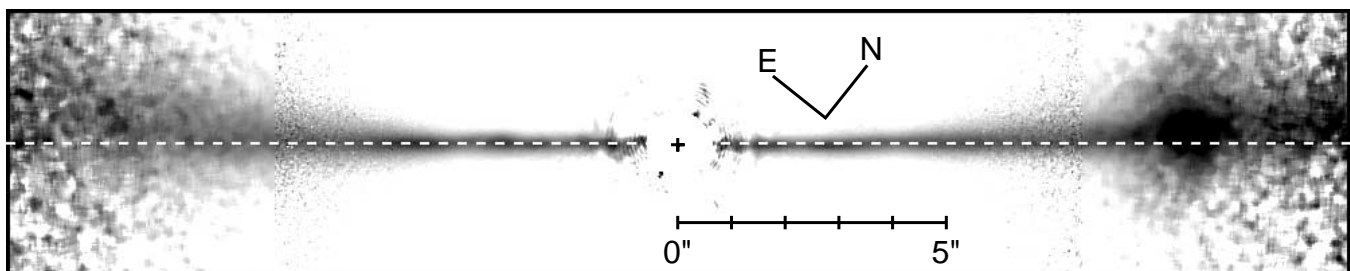


FIG. 3.—First-epoch ACS F606W coronagraphic image of the AU Mic disk normalized by the radial brightness profile power laws described in the paper and displayed in inverse intensity. Data beyond  $7''.5$  have been median-smoothed. The “bowing” can be seen in the outer disk as an upward deviation from the horizontal line defined by the inner midplane.

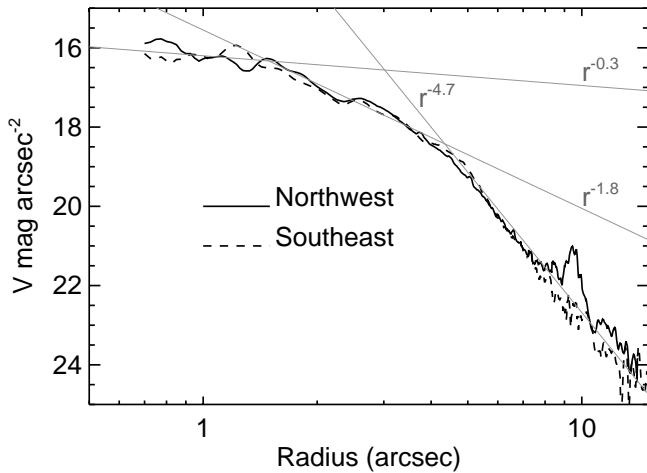


FIG. 4.—Radial surface brightness profiles following the AU Mic disk midplane (including the bow) measured over  $0''.25 \times 0''.25$  subapertures in the first-epoch ACS F606W coronagraphic image. Power-law profiles are superposed.

the southeast. These angles are consistent with those reported by KLM04 and L04.

Radial surface brightness profiles along the disk midplane, accounting for the bow, are shown in Figure 4. Both sides of the disk appear to have very similar profiles, although the northwest side is brighter beyond  $10''$  (100 AU) by  $\sim 2$  times relative to the southeast. The mean midplane radial brightness profile can be reasonably divided into three zones described by different power laws. The inner zone ( $r < 1''.5$ ) is nearly flat ( $I \propto r^{-0.3}$ ). The middle zone ( $1''.5 < r < 4''.3$ ) has a moderate radial decrease in brightness ( $I \propto r^{-1.8}$ ), which is slightly steeper than that measured by L04 (from  $r^{-1.0}$  to  $r^{-1.4}$ ). The outer zone ( $r > 4''.3$ ) drops off rapidly ( $I \propto r^{-4.7}$ ), which is steeper than the  $\sim r^{-3.8}$  measured by KLM04 between  $6''$  and  $16''$  but is consistent with the  $r^{-4.4 \pm 0.3}$  reported by L04.

Localized deviations from the large-scale brightness profile are present. There are  $\sim 20\%$  dips at  $r = 2''.3$  (23 AU) on both sides that appear to be genuine and not PSF subtraction artifacts. Between  $4''.3$  and  $5''.3$  the southeast side is  $\sim 25\%$  brighter than the northwest. Within  $1''.5$  the subtraction residuals are too large to identify any localized asymmetries of less than 30%. To highlight the small-scale variations, each row in the image parallel to the midplane was divided by a smooth function, a fourth-order polynomial fit derived from the mean midplane radial brightness profile. The resulting image (Fig. 5) emphasizes the deviations and can be compared with Figure 3 of L04. The dip at 23 AU is clear, although any features closer to the star

than it are suspect. There are correlations between features in these images and those seen in the L04 data (L04 labeling convention used; distances in parentheses are the centers of the features as seen in the L04 image): (A) a “clump” at 26 AU (25 AU), (B) a dip at 29 AU (29 AU), and (C) a clump at 33 AU (31 AU). The relatively large discrepancy in the position of feature C between the *HST* and L04 data may be due to subtraction errors in either or both data sets. We note that the positions of the features appear the same in the *HST* images at both epochs. At 37 AU on the northwest side there is a marginal enhancement that may correspond to L04’s clump D, whereas at the same radius in the southeast side there is a slight dip. Beyond that radius the northwest side smoothly declines, but there is one more extended clump at 48 AU in the southeast.

The inner disk’s vertical brightness profile (Fig. 6) shows a sharp midplane with extended wings. It can be reasonably well characterized for disk radii less than  $5''$  by a Lorentzian profile:  $I(z) = 1/(1 + z^2/h^2)$ , where  $2h$  is the profile FWHM and  $z$  is the height above the midplane. Note that we find this particular shape to be a convenient description of the disk profile and do not assert any physical significance to it. The profiles are generally symmetric about the midplane for  $r < 5''$ , but beyond this the disk is brighter on the northeast side of the midplane. The outer disk profile is more rounded, lacking a sharp midplane.

The FWHM at each radius was measured by fitting a Lorentzian profile to a vertical cross-section of the image after smoothing by 5 pixels along the direction of the midplane. As shown in Figure 7, the inner disk is rather flat, but the outer disk begins to rapidly broaden beyond  $5''$ . The FWHM for  $r < 5''$  (50 AU) is  $0''.25$ – $0''.35$  (2.5–3.5 AU). At  $r = 7''.5$  (75 AU) the FWHM on the southeast side is  $0''.9$  (9 AU) and  $0''.65$  (6.5 AU) on the northwest. The change in FWHM along the southeast side can be approximately described by two power laws:  $\text{FWHM} \propto r^{0.07}$  for  $1''.5 < r < 4''.6$  and  $r^{2.4}$  for  $4''.6 < r < 7''.5$ . The equivalent relations for the northwest side are  $\text{FWHM} \propto r^{0.07}$  for  $1''.5$ – $3''.0$  and  $r^{1.0}$  for  $3''.0$ – $7''.5$ . These apparent vertical profiles represent the projection of the optically thin disk along the line of sight convolved with the instrumental PSF.

### 3.2. Disk Modeling

Derivation of the physical distribution and properties of the dust in the disk directly from an image is prohibited by the integrated effects of forward scattering and density variations seen along the line of sight. They can be estimated from three-dimensional scattering models optimized to match the observed image. We have attempted to derive a reasonable set of model parameters that match the major features of the disk in the

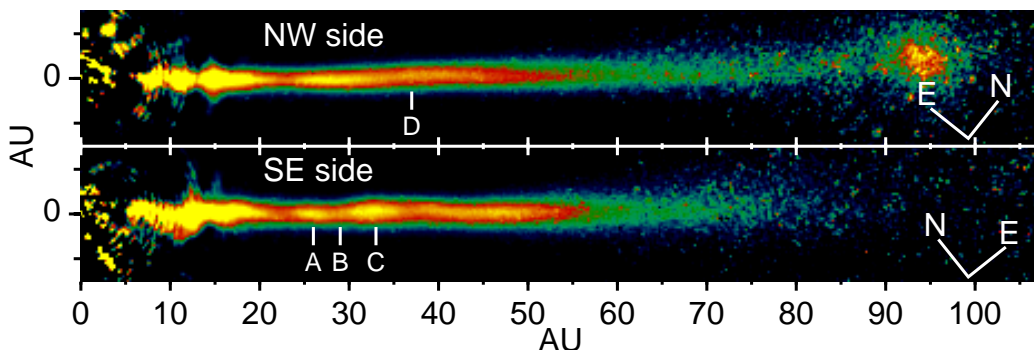


FIG. 5.—AU Mic disk ACS F606W image divided by a smooth function fitted to the midplane to highlight localized variations. The southeast side has been flipped about the star for easier comparison.

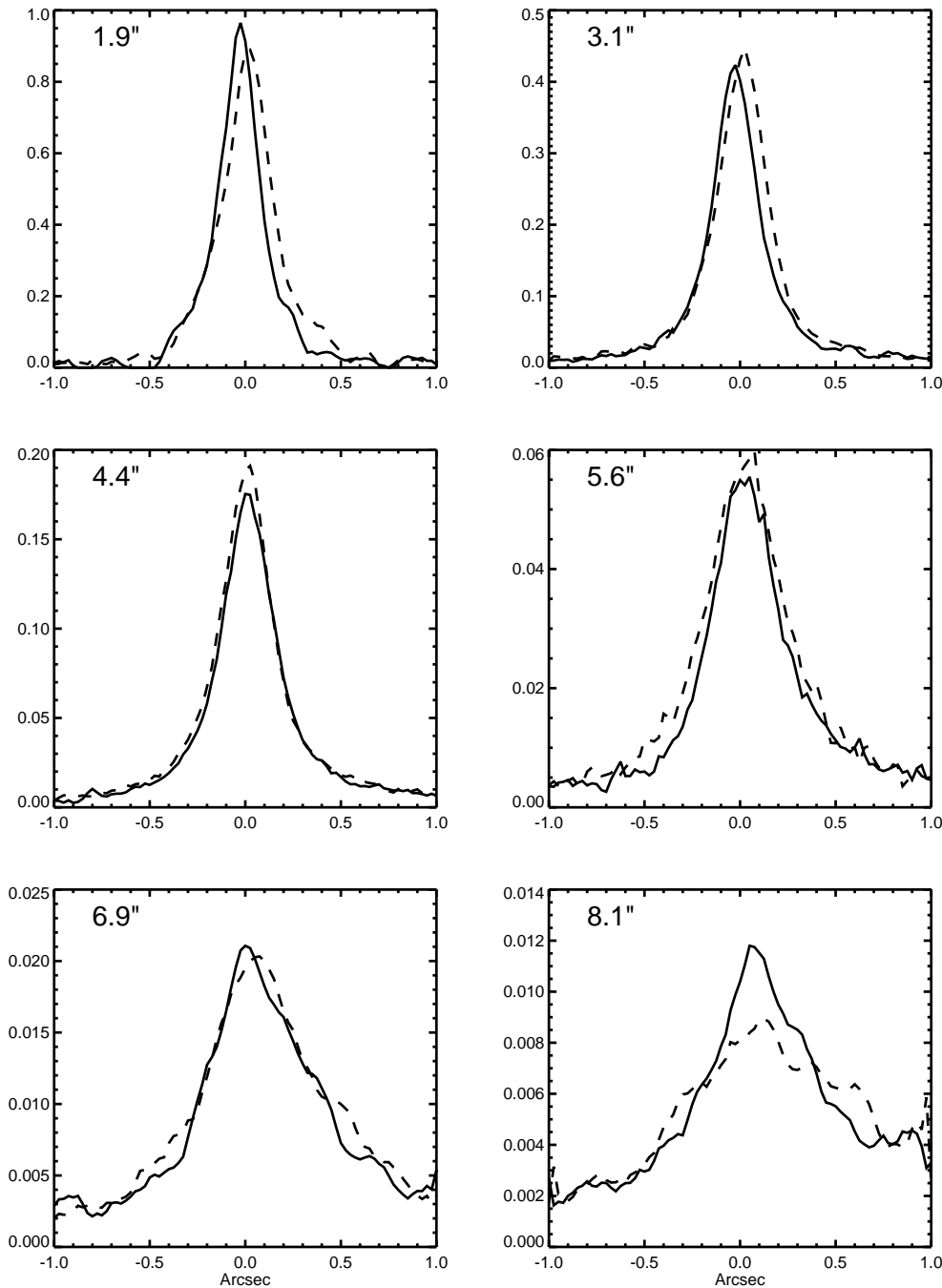


FIG. 6.—AU Mic disk intensity cross-sections perpendicular to the midplane at various radii from the first-epoch ACS F606W coronagraphic image. The solid lines represent the northwest extension of the disk and the dashed lines the southeast. The northeast side of the disk is toward the right. The disk bow can be seen as the shift in flux toward the northeast at larger radii.

first-epoch F606W exposure. We emphasize that we have not fully explored the parameter space, which is likely to have some degeneracies that prevent determination of a unique set of optimal values.

The modeling code computes the singly scattered reflected light from the disk integrated along the line of sight. Because the AU Mic disk is optically thin (KLM04), nearly all of the observed light is singly scattered, and the fraction of multiply scattered photons should be insignificant. Assuming axial symmetry, the scattering surface density  $\rho(r, z)$  at radius  $r$  and height  $z$  is characterized by  $\rho(r, z) = \rho_0(r/r_0)^\alpha \phi(z, h)$ , where  $\rho_0$  is the midplane scattering density at some fiducial radius  $r_0$  and the scale height of the vertical distribution profile  $\phi(z)$  varies as  $h = h_0(r/r_0)^\beta$ . An

albedo of 0.5 is assumed. We used a Lorentzian vertical density distribution profile in which  $\phi(z) = 1/[1 + (z/h)^2]$ . The code can compute a model with contiguous annular zones, each with independent  $\alpha$ ,  $\beta$ , inclination, midplane position angle, and outer radius (the outer radius of one zone defines the inner radius of the next). The midplane densities and scale heights are constrained to be equal at the interface between two zones. The inner radius of the innermost zone is also defined, allowing for a clear central region. The intensity of reflected light from each point in the three-dimensional model is modified by the Henyey-Greenstein scattering phase function. The scattering asymmetry parameter  $g$  defines how forward-scattering the grains are ( $g = 0$  is isotropic,  $g = 1$  is fully forward-scattering).



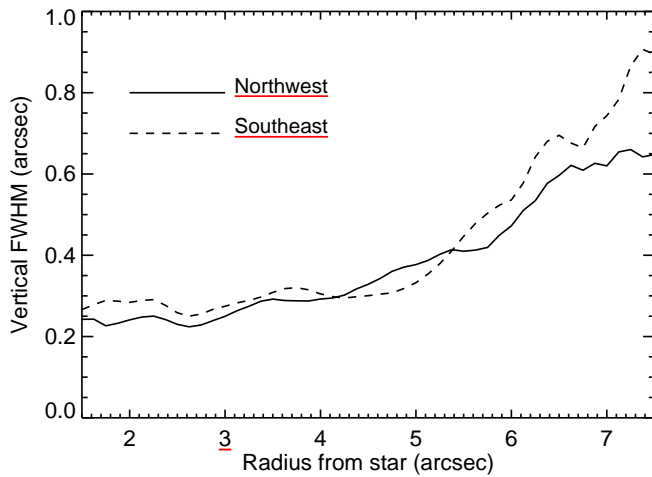


FIG. 7.—AU Mic disk FWHM measured from the ACS F606W coronagraphic image.

An iterative, nonlinear least-squares fitting routine was used to optimize the disk parameters by generating models and comparing them with the image. Both sides of the disk were simultaneously fitted using the model, which is symmetric about the star within each disk zone. To avoid the brighter inner regions from completely driving the results, the weights for all of the pixels at each radius were multiplied by the inverse of the peak midplane intensity at that radius. Regions covered by the galaxy at  $r = 9''.6$  and within  $0''.75$  of AU Mic were given zero weight. The disk model was convolved with a Tiny Tim PSF model (Krist & Hook 2004)<sup>16</sup> to account for instrumental blur. During the comparisons pixels at  $r > 7''.5$  in both the data and model were smoothed using a 7 pixel  $\times$  7 pixel median filter to reduce the noise in those faint regions. The apparent disk midplane is sufficiently extended at those radii to be unaffected by this smoothing. All of these models were computed with a 250 AU outer radius and 25 AU maximum height.

<sup>16</sup> The Tiny Tim software and manual are available at <http://www.stsci.edu/software/tinytim/>.

The model disk was initially composed of three annular zones (1–3) surrounding an inner clearing. The inner radius was somewhat arbitrarily set at 3 AU, within the masked central region. The outer radii (which were free parameters) of the zones 1, 2, and 3 were set to 14, 45, and 250 AU, respectively, corresponding to the regions defined by the power-law descriptions of the radial brightness profile. The starting values of  $\alpha$  were 0.0 for the two inner zones and  $-4.0$  for the outer. Likewise,  $\beta$  was started at 0.0 for the two inner zones and 2.0 for the outer. The values of  $h_0$  and  $\rho_0$  were determined by trial-and-error adjustments until a reasonable initial model was produced. Separate fits were made with  $g$  starting at 0.0, 0.3, and 0.6. In these runs the zones were constrained to have the same inclination (starting at 0.0) and position angle. We refer to these simple three-zone models collectively as model 1.

The first runs indicated that zone 1 was essentially clear, as the values for  $\alpha$  in all of the fits were extremely large, corresponding to a very rapid density increase at the outer boundary of the zone. The values of  $g$  were 0.45–0.65, and the inclination offsets from edge-on were  $0^\circ$ – $0.8^\circ$ . The values for  $\beta$  varied chaotically for the inner two zones, and the (data – model) residuals showed that the localized variations were likely causing difficulties in determining  $\beta$  there. In the outer zone  $\beta = 2.1$ – $2.6$ . None of the resulting models reproduced the bow or the change in the vertical profile shape between the inner and outer disk, so these fits were not deemed acceptable.

A new fit was made with some modifications to the zone layout. First, zone 1 was removed and replaced with an expanded inner clearing with an initial outer radius of 14 AU. A new zone with an initial outer radius of 85 AU was inserted between the outer two zones in order to provide more freedom to fit the transition region between the inner and outer disk. Finally, each zone was allowed to have its own inclination and position angle. We refer to this more complicated model as model 2. As before, separate fits were run with  $g$  starting at 0.0, 0.3, and 0.6 and with the same initial parameters as model 1.

Although they cannot match the small-scale variations in the disk (Fig. 8), the new fits provide improved models that reproduce the bow (Fig. 9), the radial brightness profile (Fig. 10), and the change in the vertical profile shape with radius (Fig. 11).

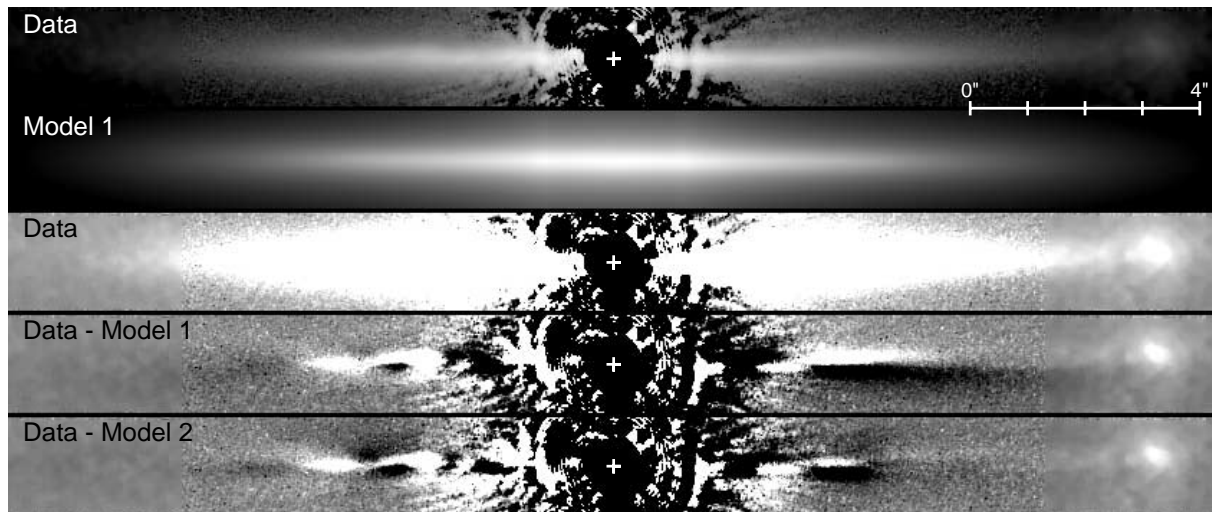


FIG. 8.—Comparisons of the AU Mic disk ACS F606W image with three-dimensional scattering models. The top two images show the observed data and the simple, three-zone model (model 1) displayed with the same logarithmic intensity stretch. Below them are the observed image and the (data – model) difference images displayed with the same strong linear stretch. Model 2 is the more complex model in which each zone can have different inclinations. The cross marks the position of the star. Data beyond  $7''.5$  are median-smoothed. Same orientation as Fig. 1.

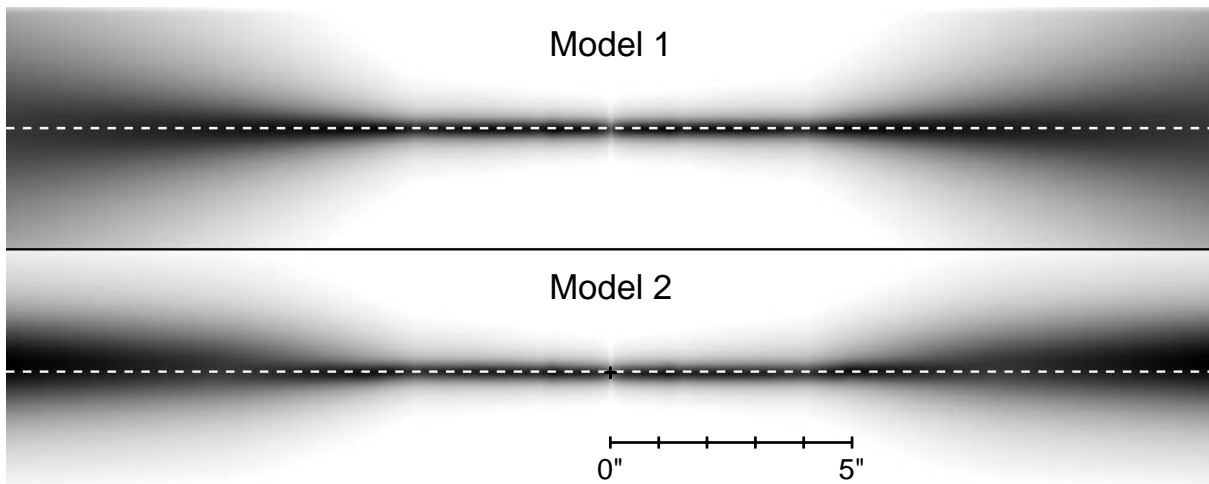


FIG. 9.—Model 1 (coplanar zones) and model 2 (independently inclined zones) displayed with inverse intensities, showing how model 2 better reproduces the disk bow (the outer disk midplane appears offset toward the top). This can be compared with the observed bow shown in Fig. 3 (same orientation as Fig. 3).

The parameter ranges are given in Table 3. Despite starting with significantly different parameters, the separate fits returned very similar results. The inner clearing is  $\sim 12$  AU in radius, which is similar to the  $\sim 17$  AU predicted by fitting the spectral energy distribution (Liu et al. 2004). The inner annular zone (zone 1) extends to  $\sim 49$  AU and has both a flat radial density distribution and thickness ( $\alpha$  and  $\beta$  are both approximately zero). It is quite close to edge-on ( $i \approx 0^\circ.6$ ), as is zone 2 ( $i \approx -0^\circ.5$ ). The density falls rapidly with radius over zone 2 ( $\alpha \approx -4.6$ ) while the disk thickness increases ( $\beta \approx 2.5$ ). The density falls off less rapidly over the outermost zone ( $\alpha \approx -2.6$ ) and the thickness increases slowly ( $\beta = 0$  to  $\sim 0.6$ ), but the inclination is notably greater with  $i \approx -3^\circ$  (the southwest pole is inclined toward us). The position angles of the zones are all within  $0.5^\circ$  of each other.

The model shows that forward scattering ( $g \approx 0.4$ ) and the inclination of the outer disk ( $r > 80$  AU) cause the bow. We do not believe that any other processes, such as interaction with the interstellar medium (ISM; Liu 2004) are required to explain its appearance. The disk is intrinsically quite thin, with a FWHM thickness of  $\sim 1.8$  AU at  $r = 20$  AU, compared with a projected and PSF-convolved FWHM of  $\sim 2.5$  AU. It broadens to  $\sim 6$  AU at  $r = 80$  AU. The model suggests that the outer disk may have

the same vertical profile as the inner, but because of its higher inclination it appears to lack a sharp midplane.

There is likely some trade-off between the variation in brightness with radius due to the scattering phase function and the radial density falloff as characterized by  $\alpha$ . A tighter constraint on the phase function would be possible if the disk could be seen closer to the star than is allowed with the occulting spot. The multizonal nature of the disk has been somewhat artificially decomposed into a set of separate power law descriptions that only provide constraints on the continuity of the density variation within a zone, without a rigorous physical basis for them. Given the number of free parameters, it is not possible to derive very robust values for both  $g$  and  $\alpha$  in the case of a multizonal, edge-on disk. This would not be a problem if the disk could be well resolved in thermal emission, where phase effects are not present.

### 3.3. The Disk in Different Filters

The disk appears generally similar over the wavelength range of the ACS images. However, the sharp, thin midplane (FWHM  $\approx 200$  mas) is blurred by the wavelength-dependent PSF (FWHM  $\approx 50$ – $72$  mas), so the apparent vertical profile of an intrinsically wavelength-independent disk would appear to differ among the filters. Consequently, measurements of color gradients are complicated. To examine what sort of PSF-induced variations might be expected, copies of model 2 were convolved with Tiny Tim model PSFs for each filter. These show that for a wavelength-independent disk and illuminating source the peak midplane intensity ratios at 30 AU are  $F435W/F606W = 1.05$  and  $F435W/F814W = 1.16$ , indicating that the midplane becomes more blurred at longer wavelengths because of the PSF. Conversely, more light is redistributed into the wings of the profile at longer wavelengths. At  $z > 0''.4$  above the midplane, the disk model surface brightness is up to 60% greater in F814W than F435W. When the observed images are normalized by the total disk flux in each filter (measured using the apertures and aperture corrections described below), the peak midplane brightnesses are equal to those predicted within the measurement errors, indicating that there are no significant intrinsic color variations with disk height.

The overall disk color was derived by computing fluxes within regions that encompass most of the disk's light. The PSF-convolved models show that by summing the flux within a  $4''.3$  long by  $0''.9$  high box aligned along the midplane and

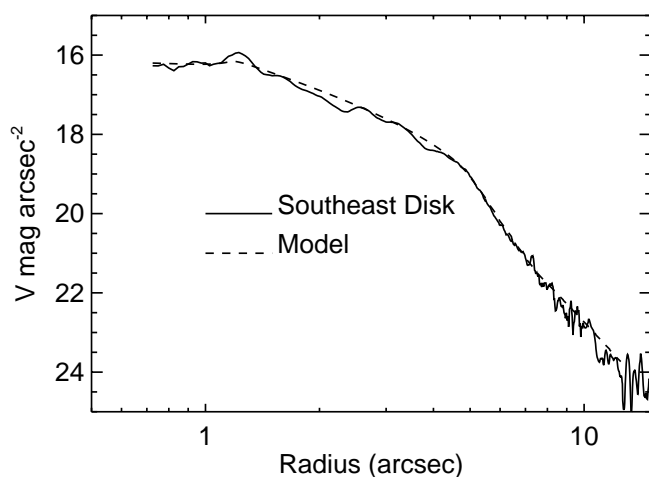


FIG. 10.—Comparison of the ACS F606W radial surface brightness profiles of the southeast side of the disk and the equivalent section of the final model.



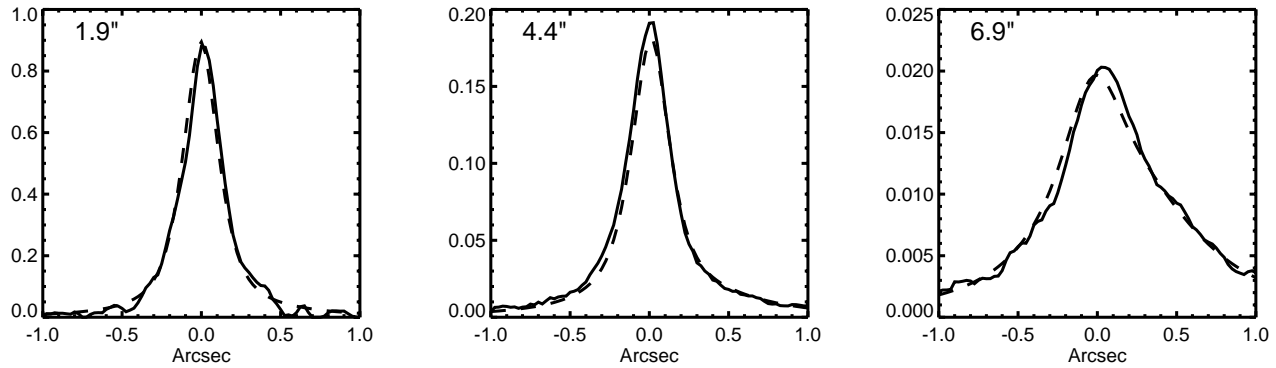


FIG. 11.—AU Mic disk ACS F606W observed and model intensity cross-sections perpendicular to the midplane at various radii. The solid lines are the southeast disk, and the dashed lines are from the model. The northeast side of the disk is toward the right.

centered at  $r = 4''.2$ , the total flux in F435W would be 1.02 times greater than in F606W and 1.09 times greater than in F814W for a neutral disk and central source. These dimensions were chosen on the basis of the region of significant signal in the observed F435W image. The same box applied to each side of the disk in the observed images indicates that the disk is blue relative to the star. After aperture corrections derived from the models, the F435W/F606W flux ratios relative to the star are 1.13 (northwest) and 1.15 (southeast), and for F435W/F814W they are 1.35 (northwest) and 1.44 (southeast). The estimated measurement error for this box size is 3%, so it appears that the disk may be slightly more blue on the southeast side. The southeast/northwest brightness asymmetry appears to decline toward longer wavelengths. The southeast/northwest brightness ratios measured within the boxes are 1.11 (F435W), 1.09 (F606W), and 1.04 (F814W). As a consistency check, the flux ratios in the April and July F606W images agree to within 1%.

The radial surface brightness profiles for each filter were computed by summing over  $1 \text{ pixel} \times 35 \text{ pixel}$  apertures at each radius centered on the midplane with aperture corrections derived from the models. The ratios of these profiles indicate that the disk becomes increasingly blue at larger radii, at least for  $r = 30\text{--}60 \text{ AU}$ . On the southeast side the F435W/F814W brightness ratio is 1.3 at 30 AU and 1.6 at 60 AU from the star.

On the northwest side the change is not as great, increasing from 1.25 to 1.45 over the same range. There is no significant color gradient seen in the F435W/F606W ratios. Within 30 AU of the star the disk appears to become more blue toward smaller radii at about the same rate. High PSF subtraction residuals in F814W may bias the results and render this trend suspect.

### 3.4. Differences between Epochs

AU Mic has a high proper motion of nearly  $0''.5 \text{ yr}^{-1}$ . The two F606W images are separated by over 4 months, so it is possible to distinguish background objects from anything that may be comoving with the star. There is nothing in the images except for the disk that appears to be associated with AU Mic. Both the galaxy seen along the midplane and the star southwest of the disk moved relative to the disk by an amount and direction consistent with the proper motion of AU Mic.

## 4. DISCUSSION

### 4.1. Indications of an Unseen Perturber?

The  $r < 12 \text{ AU}$  clearing implied by the model fits is consistent with the  $r < 17 \text{ AU}$  one predicted by Liu et al. (2004) from the disk's infrared spectral energy distribution. Given the low luminosity of the star, it cannot be caused by dust sublimation or

TABLE 3  
AU MICROSCOPII DISK MODEL FIT PARAMETERS

Parameter	Minimum	Maximum
Midplane scattering cross-section density ( $r = 20 \text{ AU}$ ) ( $\text{cm}^2/\text{cm}^3$ ) .....	$1.117 \times 10^{-15}$	$1.120 \times 10^{-15}$
FWHM thickness (AU) at $r = 20 \text{ AU}$ .....	1.73	1.74
Scattering asymmetry ( $g$ ) .....	0.372	0.374
Inner disk radius (AU) .....	11.70	11.71
Zone 1:		
Outer radius (AU) .....	48.6	49.1
Offset from edge-on (deg) .....	0.56	0.57
$\alpha$ .....	-0.066	-0.053
$\beta$ .....	0.074	0.085
Zone 2:		
Outer radius (AU) .....	78.9	82.4
Offset from edge-on (deg) .....	-0.52	-0.45
$\alpha$ .....	-4.66	-4.58
$\beta$ .....	2.45	2.52
Zone 3:		
Outer radius (AU) .....	250	250
Offset from edge-on (deg) .....	-2.97	-2.93
$\alpha$ .....	-2.68	-2.31
$\beta$ .....	0.01	0.59

expulsion of grains by radiation pressure (KLM04). As Liu et al. suggest, tidal interaction of the dust with an unseen companion within the clear zone is a strong possibility. They report no detection of an infrared companion during a “shallow” search using adaptive optics on Keck, so deeper imaging is certainly warranted. Given the nearly exact edge-on orientation of the disk, AU Mic is also a good candidate for detecting potential planetary transits.

A low-mass perturber may also explain the asymmetries and localized variations and the inclination difference between the inner and outer disk. This latter appears equivalent to the warping seen in the  $\beta$  Pic disk, which has been explained using hypothetical companions (Augereau et al. 2001). Although the tilt of the  $\beta$  Pic outer disk relative to the inner disk is mostly in the plane of the sky, in AU Mic’s disk it appears inclined mainly along the line of sight. Coincidentally, the tilt between  $\beta$  Pic’s inner and outer disks is about  $3^\circ$ , the same as for AU Mic’s.

#### 4.2. The Vertical Density Distribution

The AU Mic disk is thin, with an intrinsic FWHM derived from the model fits of  $\sim 1.9$  AU for  $r < 50$  AU increasing to  $\sim 3$  AU at  $r = 100$  AU. For comparison, the  $\beta$  Pic disk has a projected FWHM of 15–18 AU between  $r = 20$  and 120 AU, and its intrinsic thickness at  $r = 100$  AU as derived from modeling by Kalas & Jewitt (1995) is FWHM = 7–14 AU.

We stress again that the application of a Lorentzian profile simply provides a reasonable description of the vertical density distribution, which may be intrinsically more complex (e.g., the sum of multiple Gaussian distributions of various scale heights). It may be possible that the AU Mic disk has a sharper profile and is more inclined than the fits indicate. However, a greater inclination would result in a larger top/bottom asymmetry due to forward scattering.

#### 4.3. Disk Color and Grain Properties

AU Mic is the only known debris disk that appears blue relative to the star. Other such disks are either largely neutral ( $\beta$  Pic; Paresce & Burrows 1987) or redder than the star (HR 4796, Schneider et al. 1999; HD 141569A, Clampin et al. 2003) over optical wavelengths. Those stars, however, are also A types, with much greater luminosities. A potential explanation for the blue relative color is that the grain-size distribution has a larger proportion of small ( $< 1 \mu\text{m}$ ) particles than is found in the distributions in the other disks. These smaller grains scatter more light at  $\lambda = 0.4 \mu\text{m}$  than at  $0.9 \mu\text{m}$ . The radiation pressure from A stars could rapidly blow such particles out of a surrounding disk. However, an M star such as AU Mic exerts 3–5 orders of magnitude less pressure, allowing small grains to remain (Saija et al. 2003). Perhaps solar winds may exert more outward pressure on the dust than radiation in late-type stars.

The possibility that the outer regions of the disk would be blue relative to the inner was suggested by KLM04. In the absence of gas or significant radiation pressure, Poynting–Robertson drag is the dominant force in altering the location of collision-produced grains within the disk. Small grains in the inner disk should feel the most drag and migrate quickly into the star, leaving a relative abundance of larger grains there. At greater distances from the star, small grains would encounter less drag and have longer lifetimes, increasing their proportion relative to the larger grains and thus increasing the amount of light scattered at shorter wavelengths.

Forward scattering places some constraints on the inclination, as greater tilt would cause the disk on the forward side of the midplane to become significantly brighter than on the other. The scattering phase parameter value of  $g \approx 0.4$  implies that the grain population is different from those found in optically thick disks around younger stars such as HH 30 (Burrows et al. 1996), where  $g \approx 0.65$  in the visible and the grain-size distribution is probably similar to the ISM. The value of  $g$  does lie within the 0.3–0.5 range derived for  $\beta$  Pic by Kalas & Jewitt (1995) and is slightly more than the 0.25–0.35 range of HD 141569A (Clampin et al. 2003).

### 5. CONCLUSIONS

The disk of AU Mic has been imaged in scattered light at high resolution with *HST* in *BVI*-like passbands to within  $\sim 0''.5$  (5 AU) of the star. The surface brightness profiles of the two sides of the disk are generally similar, especially when compared with those of the  $\beta$  Pic disk, but localized brightness asymmetries are seen, especially in the southeast side. The disk at  $r > 100$  AU is  $\sim 2$  times brighter in the northwest than the southeast. The disk is blue relative to the star, perhaps indicating a relative surplus of small particles compared with grain-size distributions in neutral or red disks seen around earlier type stars. The radiation pressure from a late-type star like AU Mic may be insufficient to force these small grains out of the disk. An extended feature at  $r = 96$  AU on the northwest midplane is a background galaxy.

Modeling indicates that the inner ( $r < 50$  AU) region is seen very close to edge-on ( $\theta < 1^\circ$ ), whereas the outer is inclined  $\sim 3^\circ$  toward us. The disk appears to be clear of material within 12 AU of the star, consistent with the infrared spectral energy distribution. The disk has a fairly sharp midplane with an intrinsic vertical FWHM of less than 1 AU at  $r < 50$  AU that increases to  $\sim 3$  AU at  $r = 100$  AU. The degree of forward scattering by the grains is comparable to that seen in other debris disks, namely,  $\beta$  Pic.

The ACS instrument was developed under NASA contract NAS5-32865, and this research was supported by NASA grant NAG5-7697.

### REFERENCES

- Augereau, J. C., Nelson, R. P., Lagrange, A. M., Papaloizou, J. C. B., & Mouillet, D. 2001, *A&A*, 370, 447  
 Barrado y Navascués, D., Stauffer, J. R., Song, I., & Caillault, J.-P. 1999, *ApJ*, 520, L123  
 Burrows, C. J., et al. 1996, *ApJ*, 473, 437  
 Clampin, M., et al. 2003, *AJ*, 126, 385  
 Cutispoto, G., Messina, S., & Rodonò, M. 2003, *A&A*, 400, 659  
 Gilliland, R. L. 2004, ACS CCD Gains, Full Well Depths, and Linearity up to and beyond Saturation (ACS Instrum. Sci. Rep. ISR 04-01) (Baltimore: STScI)  
 Kalas, P., & Jewitt, D. 1995, *AJ*, 110, 794  
 Kalas, P., Liu, M. C., & Matthews, B. C. 2004, *Science*, 303, 1990 (KLM04)  
 Krist, J. E., & Hook, R. 2004, Tiny Tim Users Manual, Version 6.2 (Baltimore: STScI)  
 Liu, M. C. 2004, *Science*, 305, 1442 (L04)  
 Liu, M. C., Matthews, B. C., Williams, J. P., & Kalas, P. G. 2004, *ApJ*, 608, 526  
 Paresce, F., & Burrows, C. 1987, *ApJ*, 319, L23  
 Pavlovsky, C., Riess, A., Mack, J., & Gilliland, R., eds. 2004, *ACS Data Handbook Version 3.0* (Baltimore: STScI)  
 Perryman, M. A. C., et al. 1997, *A&A*, 323, L49  
 Saija, R., Iati, M. A., Giusto, A., Borghese, F., Denti, P., Aiello, S., & Cecchi-Pestellini, C. 2003, *MNRAS*, 341, 1239  
 Schneider, G., et al. 1999, *ApJ*, 513, L127  
 Song, I., Weinberger, A. J., Becklin, E. E., Zuckerman, B., & Chen, C. 2002, *AJ*, 124, 514  
 Zuckerman, B., Song, I., Bessell, M. S., & Webb, R. A. 2001, *ApJ*, 562, L87